Journal of Physics:
Conference Series

PURPOSE-LED PUBLISHING™

PAPER • **OPEN ACCESS**

High-Fidelity Digital Twins of In-Service High-Pressure Turbine Blades

To cite this article: Pierluca Dessi *et al* 2025 *J. Phys.: Conf. Ser.* **3143** 012126

View the article online for updates and enhancements.

You may also like

- Quality Evaluation of Argan Oil as a Food Product Using Ultrasonic Characterization
Mohamed Ettahiri, Adil Hamine, El Houssaine Ouacha et al.
- Thermal Properties and Microstructural Assessment of Glass Composites with Epoxy Matrix for Cryogenic Applications
A. Krzak, A J Nowak, J. Frolec et al.
- Implementation and Evaluation of Bus Rapid Transit in Congested Interactions in Baghdad City
Zahraa S. Kukaz, Ali E. Jehad, Rasha H. Al-Rubaee et al.

This content was downloaded from IP address 192.167.140.79 on 06/12/2025 at 08:49

Journal of Physics: Conference Series **3143** (2025) 012126 doi:10.1088/1742-6596/3143/1/012126

High-Fidelity Digital Twins of In-Service High-Pressure Turbine Blades

Pierluca Dessi[1], Mario Carta[1,2], Roberto Putzu[1], Tiziano Ghisu[1],Shahrokh Shahpar[2]

[1]Department of Mechanical, Chemical and Materials Engineering, University of Cagliari, Italy
[2]Fluid Mechanics, Rolls-Royce plc, Derby, DE24 8BJ, UK

E-mail: pierluca.dessi@unica.it

Abstract. During their service life, film-cooled high-pressure turbine (HPT) blades of modern aero engines experience structural deformations that affect their geometry, including both the external shape and the internal cooling cavity and channels. The accuracy of residual performance assessments through computational fluid dynamics (CFD) simulations of end-of-service blades is limited by traditional scanning techniques, which are usually capable of capturing the outer geometry and not the internal one, requiring approximations such as source terms for the modelling of film cooling. This study presents a novel methodology for reconstructing the internal geometry of end-of-service blades by applying Free Form Deformation (FFD) techniques to the design-intent internal geometry. To enable high-fidelity CFD simulations, including conjugate heat transfer analyses, the deformed internal structure is integrated with the 3D-scanned external surface of the blade, enhancing the accuracy of the geometry representation. The results demonstrate that FFD-based morphing enables the creation of fully-featured digital twins of end-of-service blades.

1 Introduction

A High-Pressure Turbine (HPT) blade is subjected to various stresses and external agents throughout its life, leading to changes in its shape at different scales. These deformations impact the exterior of the blade, but also affect the interior, modifying the geometry of the cooling channels that run through the blade and vent through surface cooling holes. Such deformations impact the blade's aerothermal performance.

Studying the performance of end-of-service blades gives useful information to designers, regarding the blade's deterioration and performance loss accumulated during their operational life. In industry, end-of-service blades are often scanned after engine overhaul, to quantify the extent of in-service deterioration. However, current scanning technologies are limited to digitalizing the outer shape of the blade, and are unable to capture internal cooling chambers and channels[1] [1, 2].

Recent advancements have made it possible to easily analyzing the effects of exterior deformations in end-of-service blades, evaluating their residual performance through high-fidelity CFD (Computational Fluid Dynamics) simulations based solely on external geometry [3, 4, 5, 6, 7]. However, these studies are inherently limited by the scanning technology, thus neglecting the effects of internal deformations on

[1]As mentioned later, micro-computed tomography is a technology that enables the digitalization of internal features too, but is not routinely industrially adopted for scanning several blades

Content from this work may be used under the terms of the Creative Commons Attribution 4.0 licence. Any further distribution of this work must maintain attribution to the author(s) and the title of the work, journal citation and DOI.
Published under licence by IOP Publishing Ltd

the blade's aerothermal behavior. This approach, limited to external geometry, reduces the fidelity of the simulation, as it relies on simplified models, such as Crawford-type "strip models" [8] to surrogate the presence of cooling holes, while ignoring the impact of internal geometry deformations on the cooling flow. Furthermore, the lack of internal geometry severely impact the ability to perform conjugate heat transfer analyses. As a result, both the predictive accuracy and the amount of information that can be extracted from the end-of-service blade are compromised.

The main objective of this work is to develop a technique that can be used to recreate the internal cooling geometry of a 3D-scanned end-of-service blade, starting from the datum blade (i.e., design intent). The methodology is based on FFD (Free-Form Deformation). This deformed blade's internal structure is then merged with the 3D-scanned exterior, leading to a fully-featured version of the scanned blade geometry. To the best of the authors' knowledge, this is the first time that FFD has been employed to reconstruct the internal geometry of an end-of-service blade for high-fidelity simulation purposes. At the moment of writing, FFD-based morphing is widely used for various reverse-engineering applications, ranging from biomechanics [9] to agricultural [10] applications. In relation to turbine blades, the main application of FFD is in the optimization field [11, 12, 13].

The present article is organized as follows. Firstly, in Section 2, the methodology is described, following its procedure and highlighting the different available options (and the need of their implementation), starting from the design intent and the SLS-scanned blade, and ending with a CFD-ready fully-featured end-of-service blade. In Section 3, two test cases are presented and the methodology is applied to them. The first one (Section 3.1) is a simplified turbine rotor geometry which is methodically deformed to match an arbitrarily distorted shape. The second one (Section 3.2) is represented by a real 3D-scan provided by Rolls-Royce plc. Finally, in Section 4, the conclusions are drawn, highlighting the benefits and possible improvements.

2 Methodologies

2.1 Blade Acquisition

The blade acquisition is the process that generates the digitalized model of the end-of-service blade under-examination. The end-of-service blade is scanned using a 3D structured light scanner (SLS), which provides a point cloud representation of the blade [14]. Subsequently, the point cloud is filtered and triangulated to produce an STL file representing the end-of-service blade. With this methodology (SLS scan), the digitalized model only represents the blade's exterior surface. Therefore, the blade's internal geometry must be inferred, if required for detailed analyses.

Structured light scanning is the industry standard for this type of applications. Another technology, which enables the direct digitalization of the blade's internal features, is the micro-computed tomography (MCT) [15]. At the moment, when applied to HPT blades, MCT is mainly used for non-destructive testing (NDT) [16], while it is not adopted for large-scale scanning campaigns as with SLS.

2.2 Geometry Deformation

Methodologies to generate turbomachinery blades are usually divided between "constructive" and "deformative" methods. The former are used to generate a shape from scratch (i.e., CAD[2]-based methods) and are outside the scope of this work. The latter are used to deform existing objects. The reader is referred to the relevant literature [17, 18, 19, 20, 21, 22].

Among the deformative methods, the most common are:

- Free-Form Deformation (FFD). This method is based on defining a regularly spaced 3D lattice of control points that encapsulates the blade. Their displacements induce a smooth and continuous deformation of the blade itself [23, 12].
- Radial Basis Functions (RBF). This method employs, as the name suggests, radial basis functions to interpolate displacements defined at scattered control points. With the RBF approach, the control points can be arbitrarily numerous and arbitrarily located. RBFs are particularly effective for localized deformations, but it is also possible to model global deformations [24, 25].
- Hicks-Henne bumps. This method employs Hicks-Henne basis functions, typically used to model localized smooth bumps on the blade by defining their amplitude, position and width [23, 26].

In this work, the FFD strategy is chosen for its flexibility.

[2] Computer-Aided Design

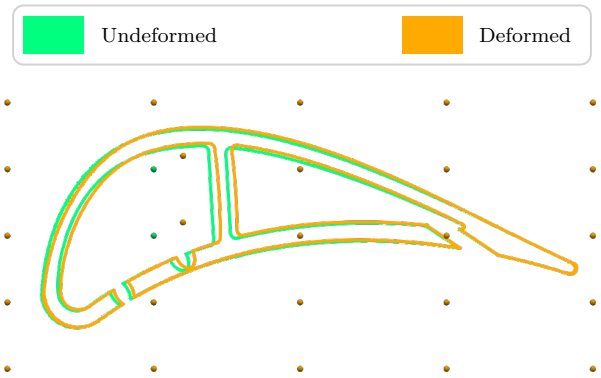

Figure 1: Geometric effects of internal control point displacements. The undeformed section and its control points are shown in green, and the deformed ones in orange.

2.3 Free-Form Deformation

Free-form deformation [18] is a method based on transferring deformations of a 3D lattice encapsulating an object to the object itself. The lattice is deformable through its control points. The deformation of the considered object (points, curves, volumes) is defined by the movement of the control points, through the trivariate tensor product of Bernstein polynomial functions (Equation 1).

$$\delta(s,t,u) = \sum_{i=0}^{l}\sum_{j=0}^{m}\sum_{k=0}^{n} b_i(s)b_j(t)b_k(u)\mathbf{d}_{i,j,k} \tag{1}$$

where b_i, b_j and b_k are the Bernstein polynomials. s, t and u are the non-dimensional local coordinates of a generic point $\overline{\mathbf{x}}$ inside the lattice (with $0 \leq s,t,u \leq 1$). $\mathbf{d}_{i,j,k}$ is the displacement of the (i,j,k) control point. Finally, $\delta(s,t,u)$ is the displacement of the generic point (at local coordinates s,t,u), subsequent to the deformation of the lattice. The generic deformed point $\mathbf{x}(s,t,u)$ is then obtained (Equation 2).

$$\mathbf{x}(s,t,u) = \begin{bmatrix}(\overline{x}_s + \delta_s)\\(\overline{x}_t + \delta_t)\\(\overline{x}_u + \delta_u)\end{bmatrix} \tag{2}$$

where $\overline{\mathbf{x}} = [\overline{x}_s \quad \overline{x}_t \quad \overline{x}_u]$ is the previously mentioned undeformed generic point inside the lattice.

In the present work, some modifications to the standard FFD method are introduced, in order to adapt the methodology to the type of deformations encountered in scanned blades (represent only physically meaningful deformations). The main change is that not all lattice control points are used independently to apply the desired deformation. This leads to two key changes in the procedure:

- The displacements of control points internal to the lattice envelope are bilinearly interpolated using the displacements of the control points located on the lattice edges and faces at the same height (along the blade span). This enables the use of finer lattices (e.g., $3 \times 3 \times 3$ control points) without having to independently specify the position of inner control points, which could lead to unphysical interior deformations (e.g., modifying the internal region without affecting the exterior geometry). An example of the effects of freely moved inner control points is shown in Figure 1. In the presence of a minimal change in the blade surface, the internal chambers - particularly the left one - underwent significant changes in their cross-sections. This behavior is considered unphysical in the context of this work, where internal geometry deformation is assumed to result from external deformation
- The displacements of control points located on the envelope are defined using B-spline functions. This approach enables greater flexibility and allows for non-uniform control point spacing, which is useful for placing more control points near the most representative sections of the blade

In the present work, FFD serves as the framework for the transformation function between the design intent (datum) and the end-of-service blade (target), where the exact deformation field is obtained as follows.

2.3.1 Lattice Initialization The procedure starts with the initialization of the FFD 3D lattice around the design intent blade. The lattice's position and dimensions are automatically defined to encapsulate the design intent blade. The lattice can be oriented using either the blade's global reference frame (aligned with axial, tangential and radial directions) or its local reference frame (aligned with radial, chordwise and normal-to-chord directions). The rotation angle around the radial axis, required to match the mean stagger direction, is obtained via eigendecomposition of the design intent point cloud. The FFD lattice dimensionality is a selectable parameter. Its dimensionality should be chosen based on the scale of the geometric deviations observed in the test case under examination. A graphical representation of an FFD lattice can be seen in Figure 11, for the simplified test case.

2.3.2 B-Splines Approach The B-splines approach is implemented to deal with the displacements of control points near the most important areas of the blade, which is not possible with the standard FFD method due to its constraint of needing a uniformly spaced lattice.

For this purpose, B-splines are preferred over linear interpolation due to their smoother behavior, which is similar to Bézier curves based on Bernstein polynomials, as in FFD. However, Bézier curves have global support, which limits their flexibility. B-splines, instead, provide local support naturally, allowing more freedom in choosing control point locations, preserving the foundation of Bernstein polynomials.

The order of the B-spline is a selectable parameter. In this work, parabolic B-splines (order 2) are used when possible[3]. If needed, choosing order 1 yields standard piecewise linear interpolation.

Their differences are shown in Figure 2.

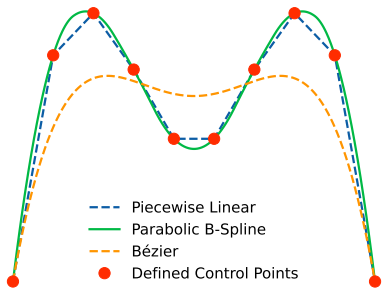

Figure 2: Interpolation of a series of control points using different techniques including piecewise linear, parabolic B-splines and Bézier curves.

The FFD lattice is initialized with a specified number of control points along each direction, chosen to accurately capture the B-spline behavior.

Since top and bottom faces represents constant-span sections of the blade, they are not governed by bivariate B-splines, instead, bilinear interpolation is applied to them. As a result, bivariate B-splines are defined only on the four lateral faces of the cuboid lattice envelope.

For each direction, the position of B-spline control lines is defined. Along the same direction, the position of B-spline control lines is kept constant. The intersections of these lines determine the positions of the B-spline control points within each lateral face. Each bivariate B-spline is then governed by the control points that lie on its corresponding face. Using control lines is preferred over directly specifying the control point positions, as it preserves a structured layout of the control points rather than having them scattered. However, this is merely an implementation choice, scattered control point configurations are also supported.

Figure 3 illustrates the concept using a $4 \times 4 \times 4$ FFD lattice, chosen to keep the figure clean and uncluttered. The four mentioned planes and control lines are highlighted.

The deformation parameters are the displacement of these B-spline control points. Given a set of deformation parameters, they are used to fit the bivariate B-splines (one per plane). These B-splines then define the displacements of the FFD control points, located on the same planes. Once this is done for all four planes, bilinear interpolation is done at each FFD's lattice height, in order to compute displacement of internal control points based on the edge values provided by the B-spline interpolation.

Figure 4 shows an example of the resulting displacements applied to a section of the lattice. To better illustrate the behavior, the same FFD lattice and B-spline control point locations as in Figure 3 are

[3]Order 2 is preferred to ensure consistency. Order 3 would require more control points and may not be feasible in some cases

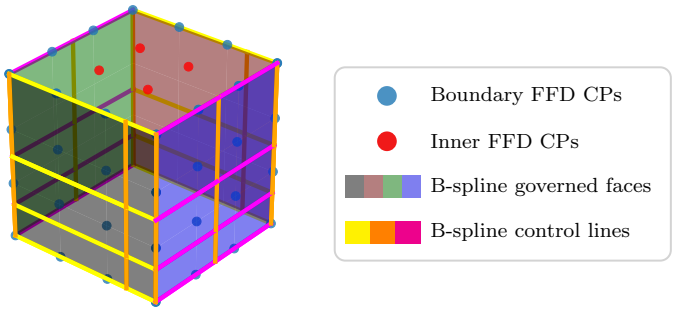

Figure 3: Exemplification of the lattice planes. FFD control points located on the lattice envelope are shown in blue, while the inner ones are shown in red. The B-spline-governed faces are highlighted in black, green, red and blue, while the B-spline control lines are shown in yellow, orange and pink.

used. For clarity, the bivariate B-spline formulation is reduced to a univariate case, where the four planes become four edges.

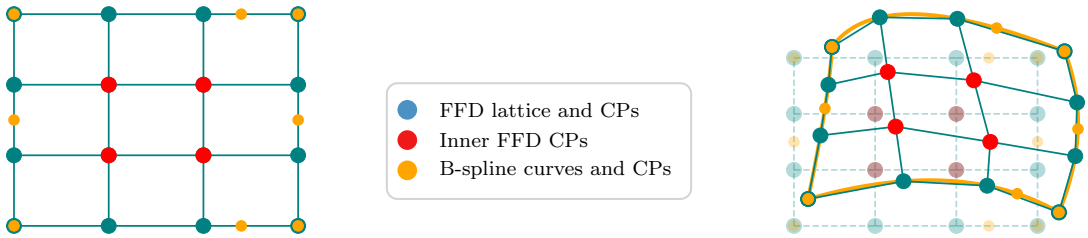

(a) Undeformed (b) Deformed

Figure 4: B-spline approach exemplification. The FFD lattice is shown in blue, with the internal control points highlighted in red, while the B-spline control points and curves are shown in yellow.

When a deformation is applied to the B-spline control points (yellow), the lattice's outer nodes (blue) are displaced according to the B-spline interpolation. The internal points (red) are then updated through bilinear interpolation based on the new positions of the outer nodes.

Altough bilinear interpolation is embedded in the procedure for its physical relevance, the B-spline step can be bypassed. In this case, the B-spline control points are placed exactly at the locations of the FFD control points. Since B-splines are constrained to pass through their control points, this configuration results in no additional interpolation effects. Therefore, moving the B-spline control points becomes equivalent to directly moving the FFD control points, as illustrated in Figure 5.

2.3.3 Engineering Deformations Approach Nowadays, engineering parametrization of airfoils and turbomachinery blades is widely used in both performance optimization [27, 28] and inverse-mapping tasks [14] as it incorporates the dominant deformation modes typically observed. As a result, it enables a reduced and more interpretable design space.

The engineering deformations approach builds upon the B-spline-based method and is used exclusively with lattices oriented in the blade's local reference frame. This choice facilitates the implementation, as it allows for an easier association between the lattice and key blade features (leading edge, trailing edge, suction side and pressure side). In this case, the deformation parameters are not the displacements of control points along each direction, but basic transformations applied to the blade sections, such as rigid body translations, rotations and recambering. These displacements are defined at each B-spline spanwise height, applied to the B-splines, and processed similarly to the B-spline-based approach.

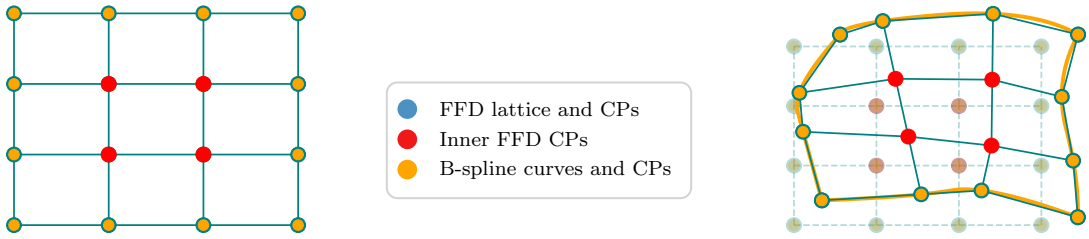

(a) Undeformed (b) Deformed

Figure 5: B-spline approach "inhibited" exemplification. As in Figure 4, the FFD lattice is shown in blue, with the internal control points highlighted in red, while the B-spline control points and curves are shown in yellow.

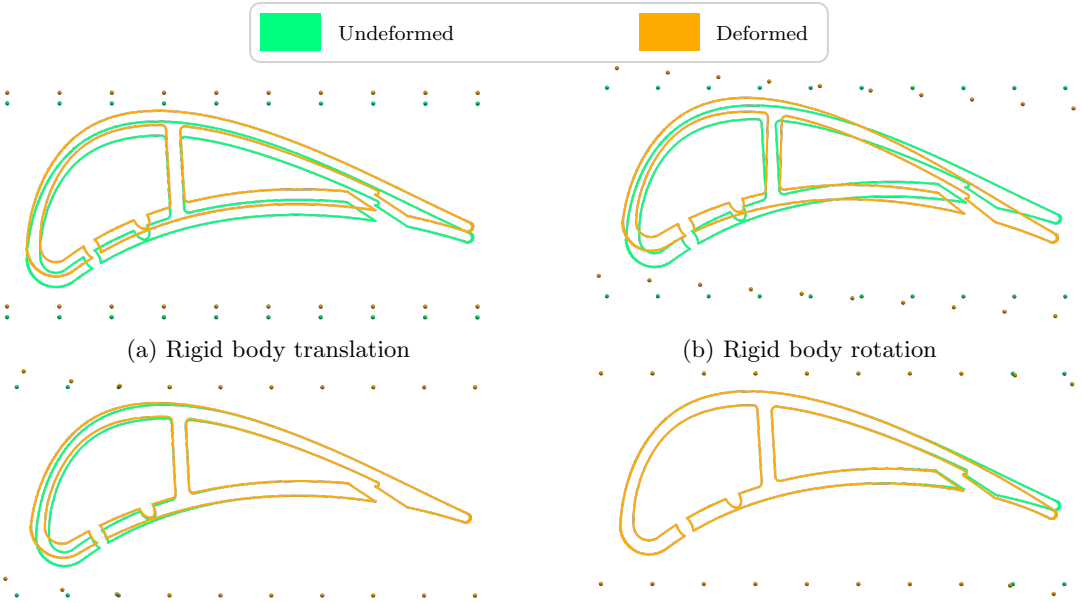

(a) Rigid body translation (b) Rigid body rotation

(c) Leading edge recambering (d) Trailing edge recambering

Figure 6: Engineering deformations exemplification. The undeformed profile and control points are shown in green, while the deformed ones are shown in orange.

The possible engineering deformations are showed in Figure 6 and a complete description is given next:

- Rigid body translations are applied by imposing the same displacement to all control points in a given section
- Rigid body rotations around the radial direction are applied using a rotation matrix, pivoting around the section's centroid, to compute the displacement of each control point
- Leading edge recambering is achieved by rotating the control points comprised between a center of rotation and the leading-edge. The center of rotation is defined as a percentage of the chord and is constrained to lie on the section's meanline[4]. The displacements are computed in two steps. First, the displacements of the extreme control points (at the leading edge) are computed using the rotation matrix. Then, the displacements of intermediate points are also computed using the

[4]The section's meanline is evaluated by computing, for each x-coordinate along the chord, the average of the n points with x-values closest to the chosen one. This enables an approximation of the meanline

rotation matrix, but the norm is scaled so that the displacement is zero at points having the same chordwise coordinate as the center of rotation. This scaling ensures that only points located between the leading edge and the rotation center are displaced, while all points aligned with or downstream of the center of rotation (i.e., toward the trailing edge) remain unaffected

- Trailing edge recambering follows the same procedure as for the leading edge, applied symmetrically at the opposite end

The scaling law governing the norm of the recambering displacements can be linear, parabolic or cubic. It is a selectable parameter, to be chosen in order to best match the target profile. Figure 7 illustrates the effect of this choice.

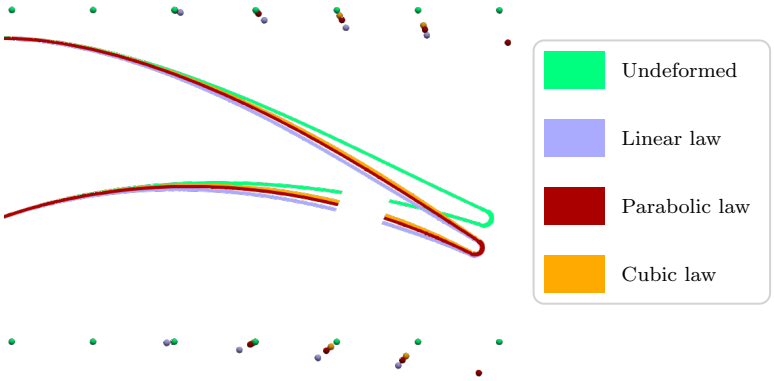

Figure 7: Effects of the scaling law for recambering. The undeformed profile and control points are shown in green, while the deformed profiles and control points are shown in purple, bordeaux and orange for the linear, parabolic and cubic laws, respectively.

The choice of implementing this type of transformations arose from limitations encountered when using the FFD B-spline method, which became evident across multiple test cases, including the real-blade configuration. As discussed in Section 3.3, the FFD approach (either with or without B-splines), led to non-physical cooling-hole displacements, i.e., changes in their curvilinear coordinates, due to control point displacements in the surface tangential direction. The engineering deformations allow to constrain the control points displacements to a more physical representation of the deformation, preventing cooling-hole displacement and variations in the blade thickness[5].

2.4 Morphing via Optimal Deformation

The morphing procedure is dedicated to obtaining the combination of deformation variables that allows the deformed design intent blade to match as closely as possible the SLS scan (target blade).

This deformation field is obtained through a minimization process based on the SLSQP algorithm [29].

The deformation variables can be, depending on the chosen method:

- The displacement of the B-spline control points along x, y, and z directions (in either the absolute or local reference frame), or restricted to the x and y directions if needed
- Engineering deformation parameters, as described in Section 2.3.3

The objective function is the sum of the unsigned L2 norms of the distances between the exterior of the design intent blade and the target blade.

The gradient evaluation is performed using forward finite differences. This method is chosen due to its lower computational cost and the similar results obtained with respect to central finite differences, as demonstrated in Figure 8. The figure shows the derivative of the objective function with respect to displacement along the axial direction (x) of a control point, for the simplified test case (described in Section 3.1), computed using forward and centered finite differences with various step sizes. This behavior is consistently observed across all deformation variables and for every tested lattice dimensionality.

[5]The change in blade thickness can be due to physical phenomena such as TBC loss or fouling, but these phenomena are not physically transferred to the blade's internal (e.g., if the blade is subjected to fouling, the cooling chambers are not enlarged). Therefore, they are not modeled in the present work.

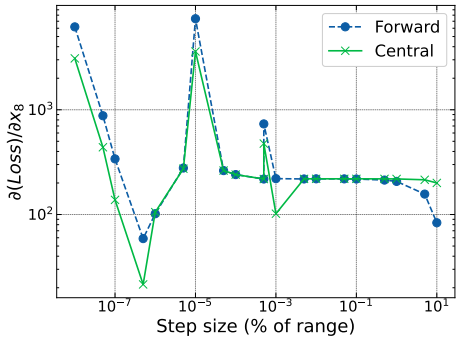

Figure 8: Finite differences comparison.

Moreover, the results shown in Figure 8 (as well as those corresponding to all other deformation variables) were also used to determine the appropriate step size for gradient computation. The goal is to identify a range of step sizes over which the computed gradient remains approximately constant, thus avoiding step sizes that are too small - leading to rounding errors - or too large - resulting in truncation errors.

For the real-blade test case the distances are computed using the P2S (Point to Surface) software, an in-house Rolls-Royce PLC tool that returns the distance field by identifying the nearest surface point of the design intent blade and measuring its normal distance to the SLS scan [14]. For the simplified-blade test case, the distances are computed using CloudCompare [30]. It is worth noting that the firtree of the blades, which is the part that engages with the rotor disk, is removed prior to morphing. This is done in order not to deform the firtree, neglecting its in-service deterioration and its impact on the performance. The control points in the lower section of the lattice are kept undeformed, in order to maintain a match between the blade and the firtree. At the end of the morphing procedure, the firtree is re-attached to the obtained blade.

The upper section of the lattice can also be constrained, in order to keep it undeformed. This is done in the real-blade test case, in order to ignore the intricate winglet's contribution to the distances. In this case, at the end of the morphing procedure, the top section is morphed using the same deformation (i.e., the same control points displacements) of the section located just below the rim.

All the codes are implemented in Python, using SciPy [31] and a modified version of PyGeM [32].

2.5 3D Scan Matching

Once the deformed internal structure is obtained, it must be trimmed to fit the SLS scan. In fact, it is not guaranteed that the deformed internal tubes precisely match the SLS scan. Additionally, the SLS scan does not have cooling holes, as the scanning process is unable to capture them and instead generates a watertight surface. This phase addresses both problems: trimming the cooling tubes to the correct length and creating holes aligned with them.

This procedure is fully automated through a custom routine scripted in Blender [33], an open-source 3D software with built-in support for scripting and automation.

The process is now illustrated. It works with the deformed internal obtained through the morphing procedure and the SLS scan. It comprises the following steps:

1. Selection of the cooling tubes and separation from the remaining part of the internal structure.

   The cooling tubes of the deformed internal structure are selected based on non-manifold boundary condition, allowing the identification of their outer extremities, i.e. the ones on the external blade's side[6]. By propagating the selection, it is possible to select the full tubes themselves and separate them from the rest of the internal structure. The separation is done primarily to reduce the computational cost of the subsequent boolean operations, which decreases due to the exclusion of the intricate geometry of the cooling chambers and the reduced number vertices considered. Additionally, it allows further separation of tubes into clusters, making it possible to perform the boolean operations consecutively (e.g., ten tubes at a time), rather than handling the complete set of tubes in a single operation, which increases RAM usage.

[6]This selection also includes lower regions where the internal channels connect to the firtree. However, these regions lie at the same spanwise position as the firtree cut, they are neglected and the selection is disabled for such points.

2. Extension of the cooling tubes.

   The cooling tubes are extended by moving all the vertices at their outer extremities along the tube axial direction by a predefined distance[7]. This is done in preparation for the subsequent operations, to guarantee that all the tubes intersect the SLS scan[8]. For each tube, the axial direction is computed as mean direction of the longitudinal edges of the STL triangles that compose it.

3. Using the extended cooling tubes to create holes in the SLS scan.

   The extended tubes are used to cut holes in the SLS scan, using boolean subtractions. At the end of this procedure, the SLS scan has holes corresponding to the vents of the cooling tubes.

4. Trimming the tubes flush with the SLS scan surface.

   The extended cooling tubes are cut flush to the SLS scan. This operation is done with two boolean subtractions. First, a negative of the SLS scan is obtained through a boolean subtraction between a cube and the SLS scan itself (more precisely, a duplicate of the SLS scan created before the step 3., in order to ensure a watertight SLS scan). The mentioned cube is automatically created to fully encapsulate the SLS scan (automatic evaluation of its position and dimensions). The extended cooling tubes are then cut to align flush with the SLS scan using the previously generated negative SLS scan.

5. Merging the cooling tubes with the remaining part of the morphed internal geometry.

   The final step involves merging the cooling tubes with the remaining part of the deformed internal structure. This is achieved by merging the vertices within a specified threshold distance. It is worth noting that, in order to obtain a fully-featured SLS scan, it is necessary to merge the internal structure with the SLS scan. Additionally, the design intent firtree must also be merged with the complete geometry. This step is optional, as the meshing procedure might require keeping the parts separate.

3 Results

3.1 Simplified-Blade Test Case

The simplified-blade test case, previously mentioned in the introduction, is described below. It is based on a design intent blade and a pseudo-SLS scan (target blade). The creation of this test case began with generating the design intent blade using CAD tools. Then, the target blade was generated by applying an artificial deformation to the design intent through CAD-based techniques. The use of a simplified geometry aimed to facilitate the development and testing of the methodology, avoiding the complexities of the real blade geometry.

Figure 9 shows a comparison of design intent and pseudo-SLS scan, with cuts at 5 span heights (0%, 25%, 50%, 75%, 100%) shown in Figure 9d to highlight the differences. Figure 10 shows the initial distance field[9]. It is worth noting that the CloudCompare script does not distinguish between suction side and pressure side of the blade, returning the minimum distance available.

For this test case, the following two approaches are tested:

1. B-splines approach (with B-spline control points coincident with FFD control points), using an oriented lattice with 5 divisions chordwise, 4 perpendicular to the chord and 5 spanwise, with displacements constrained to lie on the spanwise planes. The impacts of lattice dimensionality and orientation on the morphing performance are also investigated

2. Engineering parameters, with 5 sections, each one with the full set of available engineering parameters (rigid chordwise and normal-to-chord translation, rigid rotation, leading and trailing edges recambering), as described in Section 2.3.3

3.1.1 B-Splines Approach Results As already mentioned, for this approach, an FFD lattice dimensionality of $5 \times 4 \times 5$ is adopted, giving a total of 140 deformation variables (displacements are constrained to lie on the spanwise sections and the inner control points are bilinearly interpolated). The control point distribution is shown in Figure 11.

[7] It must be chosen as large as needed to allow all the cooling tubes to intersect the SLS scan

[8] Deformations not captured during the morphing procedure, mainly due to lack of implementation (such as thickness variations) can result in tubes not intersecting the SLS scan

[9] All distance fields are reported in terms of chord percentage and as a contour plot on the blade surface

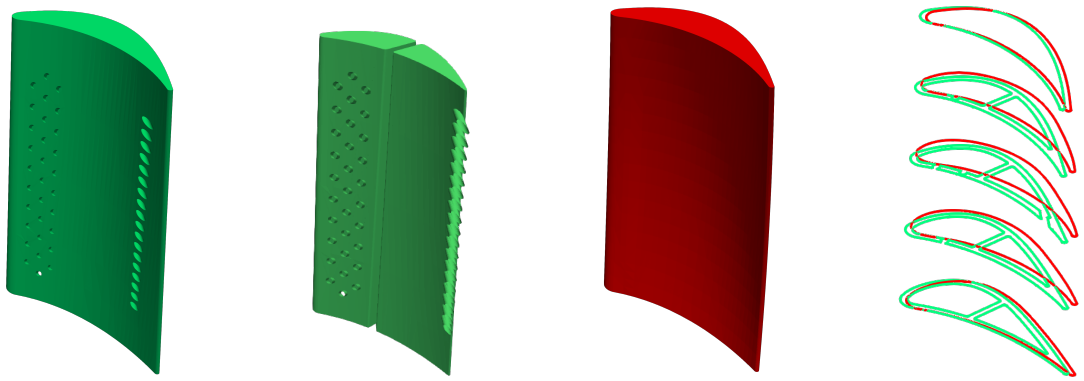

(a) Design intent blade (b) Design intent internal geometry (c) Target blade (d) Sections

Figure 9: Simplified test case.

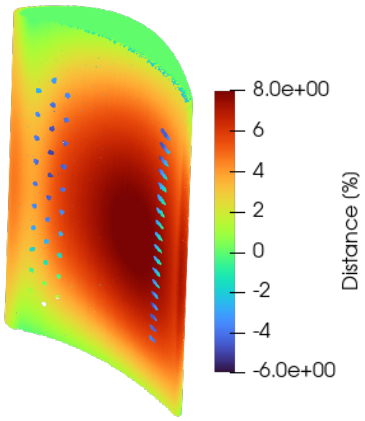

Figure 10: Starting distance field - Simplified test case.

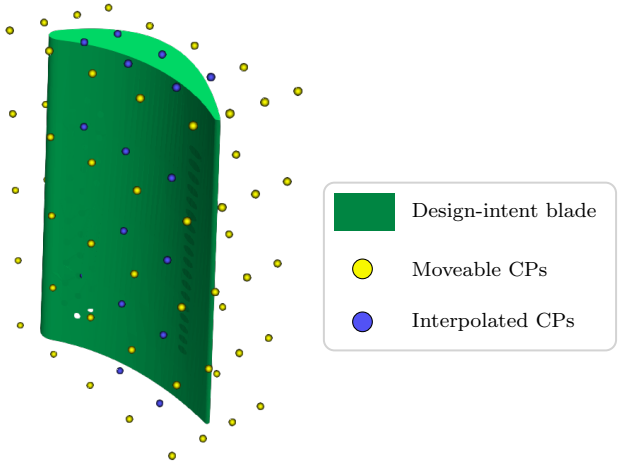

Figure 11: B-spline approach FFD control points - Simplified test case. The design-intent blade is shown in green. The moveable control points are shown in yellow, while the interpolated ones are highlighted in blue.

The history of the objective function values during the minimization is reported in Figure 12, normalized by the value of the design intent. For every iteration, at least 141 function evaluations are needed, ignoring the contribution of the line-search phase. As shown, the optimization led to a reduction of the objective function of about 98.22% of its starting value.

The whole optimization required approximately 15.750 function evaluations (including the ones for gradient evaluation and line search) and took around two hours to complete on an MSI Katana GF66 laptop (Intel i7-12700H CPU, 16 GB RAM, using 16 cores for distances computation). The optimization was terminated once the norm of the Lagrangian gradient and other optimality measures fell below the specified tolerance of $f_{\text{tol}} = 10^{-30}$ [31].

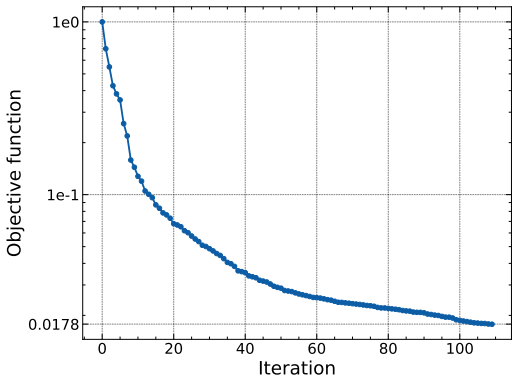

Figure 12: B-splines approach objective function history - Simplified test case. Only the iteration results are reported. Evaluations used for gradient evaluation and line search are discarted.

In Figure 13, the distance fields are reported as a contour plot on the blade surface. Figure 13a and 13b show the starting distance field and the one obtained after the optimal morphing with the same scale range, in order to highlight the differences, while Figure 13c shows the obtained distance field with scale range defined by the maximum positive and negative distances.

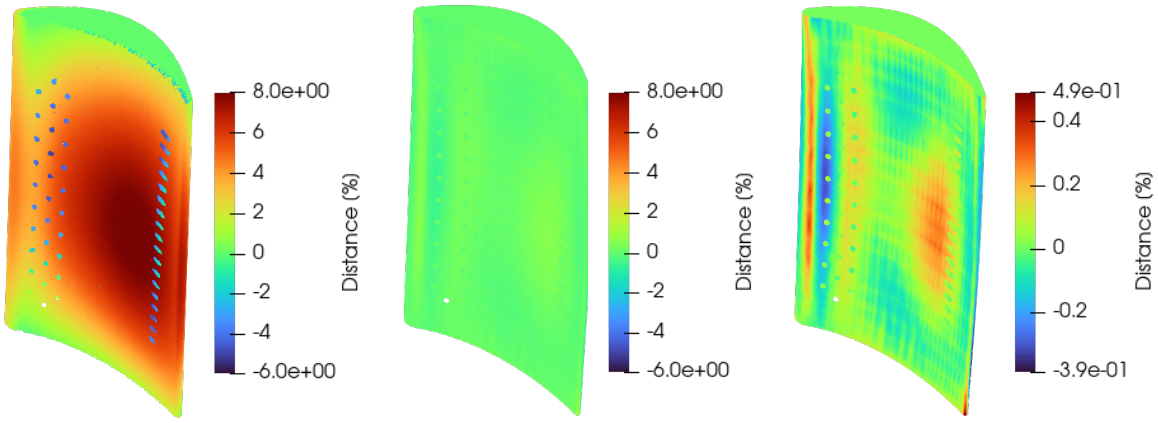

(a) Design intent vs Target

(b) Morphed vs Target - Starting scale range

(c) Morphed vs Target - Default scale range

Figure 13: Distance fields for the B-spline approach - Simplified test case.

In Figure 14a and 14b the morphed blade (internal + external) is shown, compared to the target blade, highlighting the matching between the two and the adaptation of the internal channels to the external geometry. In addition, in Figure 14c is reported the fully-featured blade (morphing + Blender refinement) compared to the design intent blade. Figure 14b and Figure 14c refer to the midspan section.

3.1.2 Dependence of Results on Number of B-Splines Control Point and Orientation Figure 15 presents a comparison between the results obtained for the simplified test case using different lattice dimensionalities and orientations, in order to assess the influence of these parameters on the outcome of the morphing

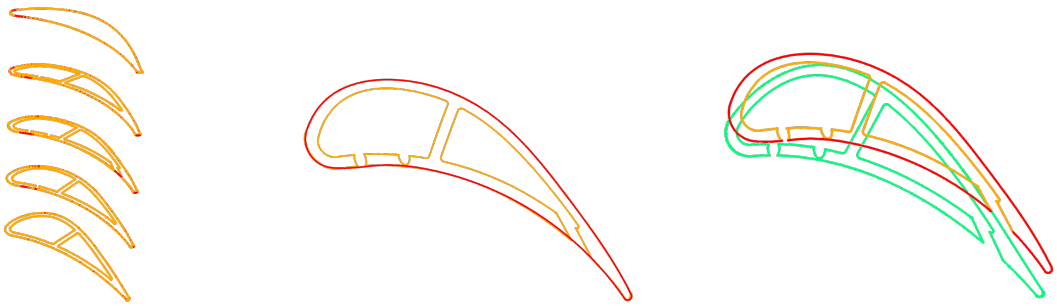

(a) Morphed vs target (b) Morphed vs target midspan (c) Fully-featured vs design intent midspan

Figure 14: Blades sections obtained with the B-spline approach, for the simplified test case. The design intent is shown in green, the target blade in red, and the morphed blade (internal + external) in orange.

process. The results are reported in terms of final objective function value as a percentage of the value of the design intent. The same stopping criteria were applied to all optimizations, consistend with the B-spline approach (Section 3.1.1). The x-axis shows the planar lattice dimensionality, i.e., the dimensionality along the x and y directions, or the chordwise and normal-to-chord directions. The legend reports the number of spanwise sections and the type of reference frame (RF). "Not Oriented" refers to a lattice oriented with the axial, tangential and radial directions, "Oriented" refers to a lattice oriented with the blade's principal directions.

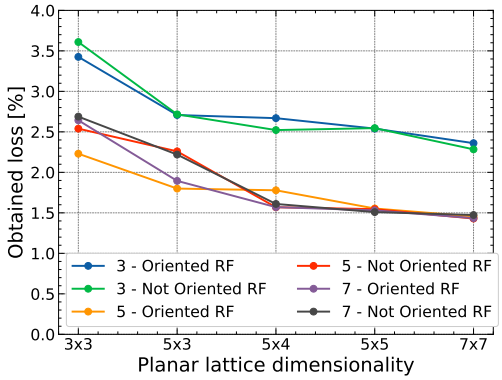

Figure 15: Dimensionality and orientation dependence.

As shown in Figure 15, using 5 spanwise sections instead of 3 leads to better loss values for every tested planar lattice dimensionality, indicating that, in this test case, 3 sections are insufficient to capture some of the blade's deformations. Going up to 7 spanwise sections led to no substantial improvements from the previous results, indicating that 5 sections are sufficient for capturing the main blade deformations.

As for the influence of the orientation, the results indicate that it has a negligible effect across all tested configurations.

It is important to highlight that the scale of variation is quite small, with the maximum and minimum obtained loss values being approximately 3.6% and 1.43%, respectively. Moreover the visual differences between the tests are minor, mainly occuring at the leading and trailing edges.

Figure 16 shows the computational cost of the optimizations shown in Figure 15, reported in terms of optimizer iterations (Figure 16a) and objective function evaluations (Figure 16b).

It is worth noting that the number of optimizer iterations does not tend to increase with the number of deformation parameters. However, the overall computational cost increases, primarily due to the additional objective function evaluations required for the gradient computation.

To summarize the relationship between computational cost C (Fig. 16b) and final loss L (Fig. 15), the morphing efficiency coefficient M_{Eff} is defined herein (Equation 3). High values of M_{Eff} indicate low loss values and/or low computational cost, while low M_{Eff} values indicate high loss values and/or

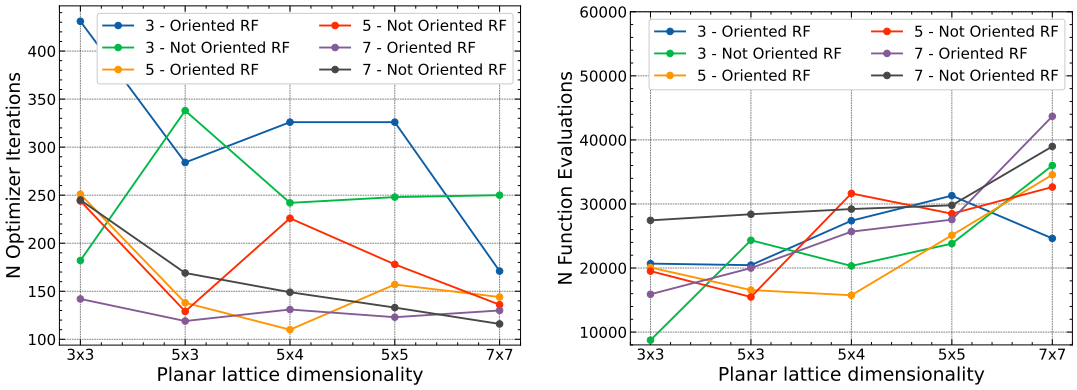

(a) Optimizer iterations (b) Objective function evaluations

Figure 16: Computatational cost of the optimizations shown in Fig. 15.

high computational cost. The terms $L_{\max}$, $L_{\min}$, $C_{\max}$, $C_{\min}$ are introduced for non-dimensionalization purposes. Its values are reported in Figure 17.

$$M_{\text{Eff}} = \frac{L_{\max} - L_i}{L_{\max} - L_{\min}} \cdot \frac{C_{\max} - C_i}{C_{\max} - C_{\min}} \tag{3}$$

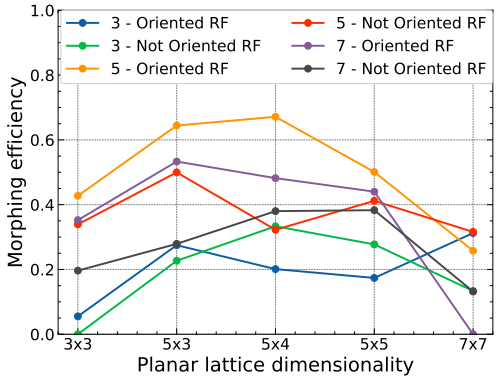

Figure 17: Morphing efficiency.

As shown in Figure 17, for this test case, the highest morphing efficiency is obtained with the $5 \times 4 \times 5$ oriented lattice, the lattice presented in Section 3.1.1.

3.1.3 Engineering Deformations Approach Results In this approach, the FFD lattice has a dimensionality of $20 \times 2 \times 30$, aligned with the local blade reference frame (20 points along the chordwise direction, 2 along the normal-to-chord direction, and 30 along the spanwise direction). To maintain consistency with the other approach and allow for a meaningful comparison, the B-spline control points are defined with a coarser dimensionality of $20 \times 2 \times 5$, meaning that engineering deformations are applied and evaluated at five distinct spanwise sections (as in Section 3.1.1). This planar dimensionality is chosen to effectively capture the engineering deformations[10]. In the normal-to-chord direction, only two divisions are used, since deformations in that direction are defined linearly, unlike the chordwise direction where recambering involves higher-order variations.

With 7 deformation parameters for each section (rigid body translations along the chordwise and normal-to-chord directions, rigid body rotation, leading and trailing edge recambering angles with their centers of rotation), this approach results in an optimization problem with a total of 35 deformation

[10]It can be increased as needed, as it does not affect the computational cost of the optimization

parameters. The history of objective function during the minimization, normalized by the value of the design intent, is reported in Figure 18.

The full optimization required approximately 2140 function evaluations (including the ones for gradient evaluation and line search) and took around 20 minutes to complete on the same MSI Katana GF66 laptop, in comparison with the 15750 evaluations and 2 hours required by the B-spline approach. The optimization was terminated once the norm of the Lagrangian gradient and other optimality measures fell below the specified tolerance of $f_{\text{tol}} = 10^{-30}$, as in the B-spline approach. It is worth noting that the number of optimizer iterations was nearly halved (56 for the eng. deformations approach versus 110 for the B-spline approach). However, the total number of function evaluations was approximately 7 times lower, mainly due to the lower number of deformation parameters, which reduced the number of evaluations needed for gradient computation.

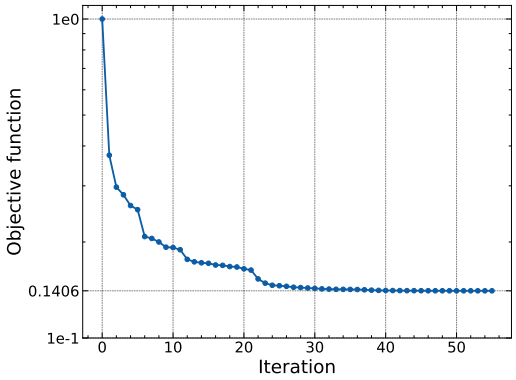

Figure 18: Eng. deformations approach objective function history - Simplified test case. Only the iteration results are reported. Evaluations used for gradient evaluation and line search are discarted.

As reported in Figure 18, the obtained objective function value is higher than the one obtained through the B-spline approach method (Figure 12). With this approach, the objective function was reduced of 85.94% of its starting value (compared to the 98.22% obtained with the B-spline approach results).

In Figure 19, the distance fields are reported as a contour plot on the blade surface. In Figure 19b the distance field is reported with the same scale range as Figure 19a, while Figure 19c shows the obtained distance field with scale range defined by the maximum positive and negative distances.

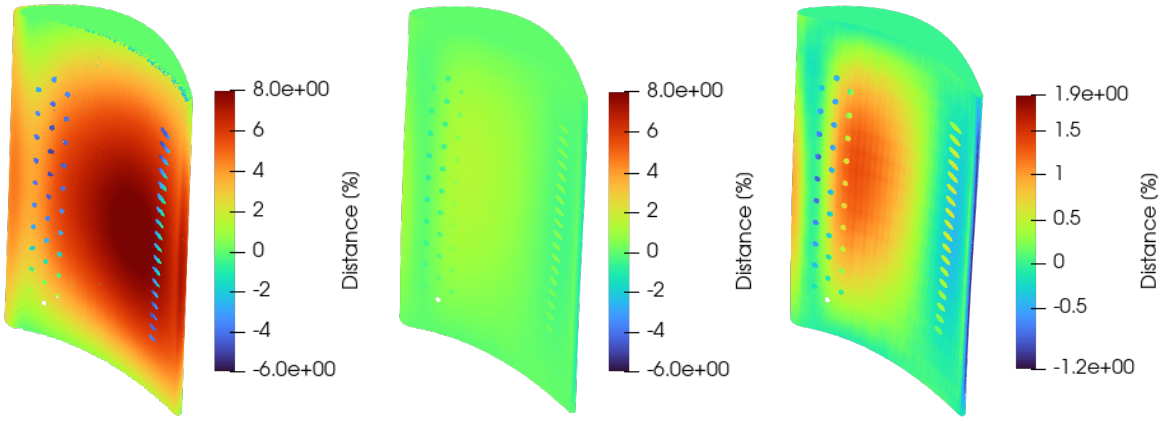

(a) Design intent vs Target

(b) Morphed vs Target - Starting scale range

(c) Morphed vs Target - Default scale range

Figure 19: Distance fields for the eng. deformations approach - Simplified test case.

Figure 20 shows the morphed blade (internal + external) compared to the target, in order to highlight the matching between the two.

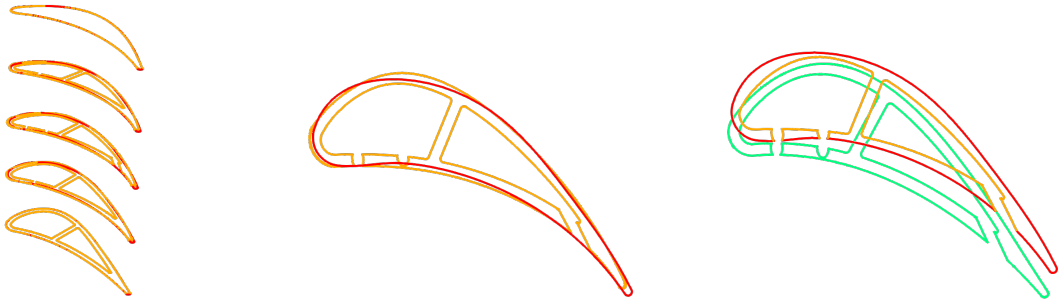

(a) Morphed vs Target (b) Morphed vs target midspan (c) Fully-featured vs design intent midspan

Figure 20: Blade sections obtained with the eng. deformations approach, for the simplified test case. The design intent is shown in green, the target blade in red, and the morphed blade (internal + external) in orange.

Looking at Figure 20c, it may appear that a new hole is generated at midspan by the central tube. However, this is caused by the tube intersecting the outer surface at midspan due to morphing inaccuracies. In the design intent geometry, this intersection occurs at a different spanwise location, but the imperfect deformation leads to a misalignment that makes the tube appear to pierce the surface at midspan.

As seen, the obtained result does not correctly capture all the geometrical differences on the external surfaces, leading to a less accurate morphing of the interior geometry. This is because the distorted geometry is affected by some engineering deformations not accounted for in the procedure, such as chord adjustments and thickness variations. These deformations are intentionally not included in the procedure due to their physical nature. For example, thickness variations - such as those caused by TBC loss or fouling - should not affect the interior geometry and therefore should not be captured. The failure to accurately match the target blade is thus attributed to the characteristics of the test case, which exhibits deformation modes and, in general, more severe deformations, than the ones usually encountered in real end-of-service blades.

The obtained objective function value could be further reduced by implementing, for example, thickness adjustments. However, the goal of this work is not to exactly reproduce the external surface, but rather to reconstruct a plausible internal geometry representative of the end-of-service blade. In light of this, incorporating thickness modeling and chord adjustments is not recommended.

3.2 Real-Blade Test Case

The real-blade test case is a modern high-pressure rotor blade, featuring a squealer-tip geometry and several film-cooling holes. The target blade is represented by a SLS scan of an end-of-service HPT rotor blade. The test case is illustrated in Figure 21. To comply with industrial confidentiality constraints, the non-dimensionalized initial distance field is shown as a contour plot on the target blade surface in Figure 21a. The distance fields, for the same reason, are shown in a blurred form. Figure 21b shows the SLS scan along with the B-splines control points, highlighting the non-equidistant spanwise sections.

For this test case, the engineering-deformations-based approach is used, since the B-spline approach exhibited issues with cooling-hole displacement (thoroughly discussed in Section 3.3).

For this case, 6 spanwise sections are used, including one located just below the rim and another at the blade tip. This configuration allows the morphing procedure to be applied while locking the displacements at the blade tip, thereby excluding the intricate winglet's contribution to the objective function. That is, distances in the winglet region are not included in the summation. After completing the morphing procedure, the displacements at the tip control points are set equal to those at the rim-section control points[11]. Additionally, the hub is also locked to ensure compatibility with the firtree. A B-spline section is added just above the hub to introduce the first active section.

Given the four active sections, results in a optimization problem with 28 deformation variables (7 deformation variables per section $\times$ 4 sections).

[11] Negleting macroscopic deformations at the tip and enforcing the same displacement as at the rim section

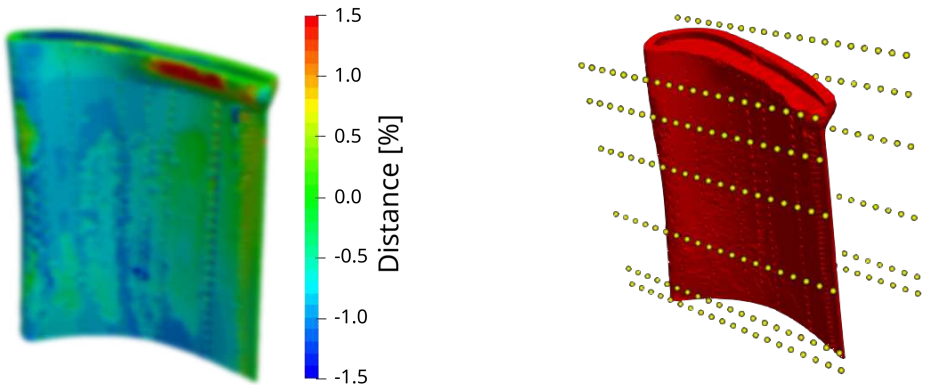

(a) Starting Distance Field (b) B-Spline control points

Figure 21: Real-blade test case. In Figure b, the target blade is shown in red, while the B-spline control points are shown in yellow. Pictures distorted. Geometry and contours intentionally blurred for industrial confidentiality reasons.

An FFD lattice dimensionality of $20 \times 2 \times 30$ is adopted, matching the one used in the simplified-blade test case.

The evolution of the objective function throughout the morphing process is shown in Figure 22, normalized by the value of the design intent. The full optimization required approximately 3900 objective function evaluations (including the ones required for gradient evaluation and line search), and was terminated when the norm of the Lagrangian gradient and other optimality measures fell below the specified tolerance of $f_{\text{tol}} = 10^{-30}$, as in the simplified test case.

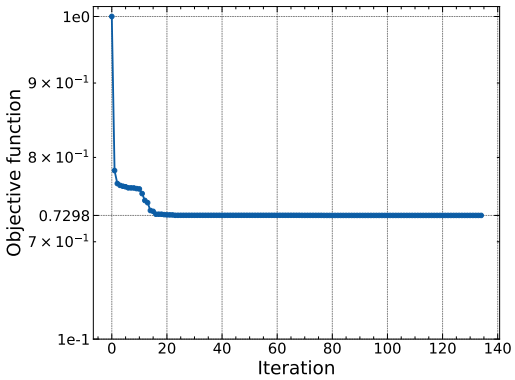

Figure 22: Objective function history - Real-blade test case. Only the iteration results are reported. Evaluations used for gradient evaluation and line search are discarted.

As depicted in Figure 22, the objective function decreased of 27.02% of its initial value.

In Figure 23, the distance fields are reported as a contour plot on the blade surface. Figure 23a and 23b shows the starting distance field and the one obtained after the optimal morphing with the same scale range, in order to highlight the differences.

As visible in Figure 22, the objective function does not achieve the same level of reduction as the one obtained in the simplified-blade test case. Several factors contribute to this:

- Due to the need to reattach the firtree, deformations at the hub section are not allowed. This penalizes the objective function reduction, as distances at the hub section affect its value but cannot be modified
- This test case exhibits surface roughness, fouling and thermal barrier coating loss, which influence the distance field. These effects are intentionally not captured by the morphing deformation

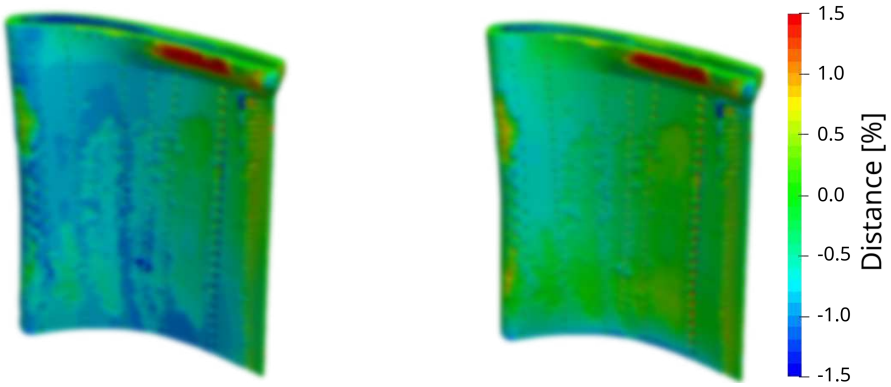

(a) Design intent vs Target (b) Morphed via optimal deformation vs Target

Figure 23: Distance fields - Real-blade test case. Pictures distorted. Geometry and contours intentionally blurred for industrial confidentiality reasons.

variables, as they do not modify the internal channels shapes. Areas like the leading edge at approximately 75% span significantly impact the objective function value, but obtaining a precise matching would come at the price of an undesired displacement of the cooling holes

3.3 Effect of Morphing on Cooling-Hole Location

3.3.1 Simplified-Blade Test Case During the dependence study (Section 3.1.2), using the B-spline approach, a problem related to the variation of curvilinear coordinates of the cooling holes was encountered. It is important to note that this behavior differs from the one caused by the absence of bilinear interpolation, discussed in Section 2.3. The former arises from changes in the curvilinear coordinates of external cooling holes, which also affect the internal geometry, whereas the latter relates to internal geometry variations not induced by external deformations. This issue arises because the optimizer may unintentionally introduce large variations in the curvilinear coordinates - mainly by moving control points tangentially to the surface - since such changes are not explicitly penalized in the loss function. This behavior appears to be largely independent of the lattice dimensionality and orientation.

To illustrate this issue, Figure 24 shows a comparison between the target blade, the blade obtained using engineering parameters (reported in Section 3.1.3), and an example blade obtained using the B-spline approach. Table 1 reports the differences in curvilinear coordinates of the cooling holes at various sections, obtained using the two deformation methods and expressed relative to the design-intent geometry.

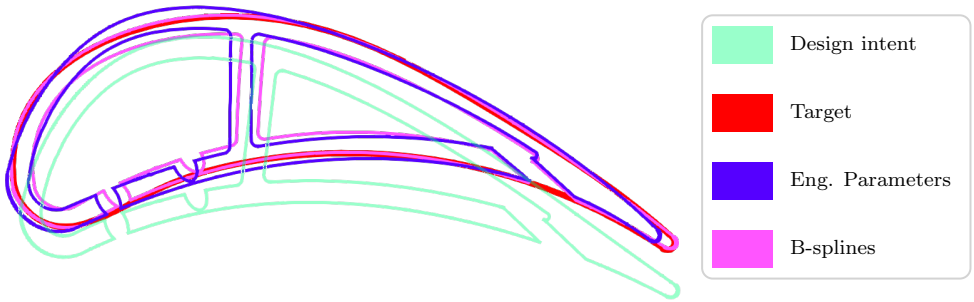

Figure 24: Example of cooling hole displacement. The blade obtained using engineering parameters is shown in blue, the one obtained using the B-spline approach in pink, the target blade is shown in red (not easily visible as it lies almost perfectly beneath the pink one), and the design intent blade in green.

As visible in Figure 24, the pink profile, morphed using the B-splines approach, correctly matches the target external geometry, outperforming the blue one, morphed using the engineering deformations approach. However, it exhibits a translation of the cooling tubes and a change in the cross-sectional area of the cooling chambers, highlighting the discussed issue. As discussed in Section 3.1.3, the less optimal match obtained with the engineering deformations approach is sufficient to capture the majority

of the deformation, and does not exhibit the same displacement of the cooling holes. Furthermore, the sub-optimal matching of the external shape is not an issue because the SLS scan will be attached to the cooling system.

Geometry	**CH 4 - H**	**CH 1 - M**	**CH 4 - M**	**CH 3 - T**	**CH 4 - T**
Eng. Deformations	1.06%	1.62%	1.18%	1.04%	0.78%
B-Spline	2.64%	3.24%	2.34%	-0.47%	-0.25%

Table 1: Differences in curvilinear coordinates of the cooling holes obtained with the two deformation methodologies, with respect to the design-intent geometry. Results are expressed as differences between normalized curvilinear coordinates (relative to trailing-edge curvilinear coordinate). CH stands for Cooling Hole; 1, 2, 3 and 4 indicate the hole number, numbered from leading edge to trailing edge; H, M and T refer to sections near the hub, midspan and tip, respectively, each selected to intersect cooling holes. (Note: not all the CH numbers are present in every section, as not all sections intersect every cooling hole)

3.3.2 Real-Blade Test Case For the real-blade test case as well, the B-spline approach was initially tested, yielding similarly good overall matching as in the simplified test case (Section 3.1.1). However, in this test case, the cooling holes experienced even larger displacements than in the simplified blade. This behavior is unphysical, because the types of deformation present on the SLS-scanned blade do not justify such a large excursion in cooling-hole position. In any case, it is expected that the section-wise curvilinear coordinates of the cooling holes do not change as a result of in-service deterioration. This issue was addressed by switching to a engineering-deformations-based morphing approach, which allowed to preserve the cooling holes' curvilinear coordinates during the deformation. This is illustrated in Figure 25, where the datum cooling holes, those resulting from the engineering-deformations-based morphing, and those from the B-spline-based morphing are shown. As visible in the figure, the holes obtained with the B-spline approach, which are displayed in pink, undergo substantial curvilinear-coordinate displacements, of the same order of magnitude of the hole diameter. Figure 25 shows the cooling holes from a view perpendicular to the blade surface, therefore, the sets of cooling holes are not expected to appear with any relative translation or shift when observed from this direction[12].

The position of the holes obtained through the engineering deformations approach, which nearly coincide with those of the design intent, confirm the method's quality in preserving their curvilinear coordinates.

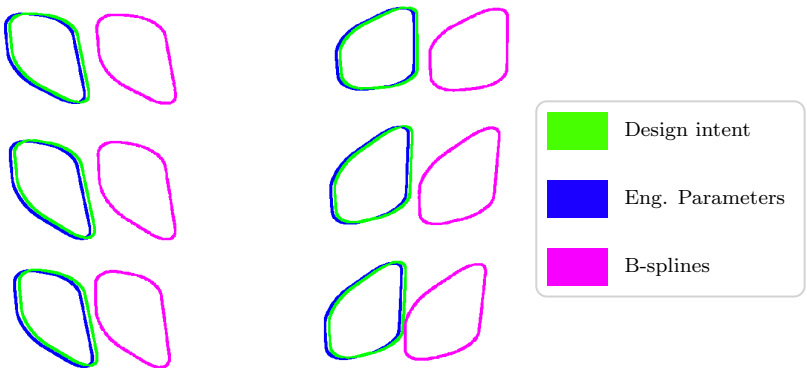

Figure 25: Cooling-hole displacements with B-spline approach on the real blade. Design-intent holes are shown in green, those morphed via the eng. parameters approach in blue and those morphed via the B-spline approach in pink. Picture distorted.

[12]The datum and target geometries are aligned, and the main deformations have limited effect in this direction

4 Conclusions

The results show that the morphing methodology developed in this work enables the deformation of the internal design-intent geometry according to the external geometry deformation, captured through 3D SLS scanning. Moreover, it provides good overall fidelity and reasonable runtimes.

A central aspect of this study is the comparison between the two developed strategies, the spline-based approach and the engineering-deformations-based approach. The former provides high flexibility, enabling accurate reproduction of the external geometry deformation. The latter allows to constrain the deformations to physically meaningful mechanisms, capturing only those deformations that are expected to be transferred to the internal geometry[13]. For instance, as previously discussed, external phenomena such as TBC loss or surface fouling affect only the outer shape. Since they do not impact the internal structure, their associated thickness variations are not captured in the engineering deformations approach, even at the cost of higher objective function values.

However, the spline-based methodology suffers from this very flexibility. The optimizer is not constrained to preserve the curvilinear coordinates of points along the blade surface, which affects the position of cooling holes, among other features. For example, even the suction side of the blade can be artificially displaced along its curvilinear coordinate, leading to variations in the cross-sectional area of the internal cooling chambers, which is unphysical within the scope of the present work.

The engineering-deformations-based methodology is introduced as an improvement over the spline-based approach. It embeds physical deformation mechanisms into the morphing process, ensuring that only plausible, structurally-relevant deformations are applied to the internal geometry. While this limits the method's ability to precisely match the external scanned geometry - as observed in the test cases - it is important to emphasize that the goal of this work is not to reproduce the external surface exactly. Rather, it is to reconstruct a plausible internal geometry representative of the end-of-service blade, which is not directly accessible.

In the simplified test case, the results obtained with the engineering-deformations approach appear less satisfactory, primarily because the geometry includes large thickness variations - more extreme than those typically observed in real end-of-service blades.

In the real-blade test case, the results obtained using the engineering-deformations approach are instead satisfactory. Altough the objective function is not significantly reduced, this does not directly indicate poor morphing procedure. The distance field clearly shows that the main trend of macroscopic blade deformation is captured, and so the deformation of the internal geometry.

One key limitation of the present work is that strong asymmetrical "microscopic" deformations (e.g., between the suction and the pressure side) may lead the optimizer to favor one side over the other, rather than converging toward a "mean" configuration. This is due to the limitation of the distance metric, which does not distinguish between microscopic and macroscopic deformations.

Regarding future work, the authors aim to perform high-fidelity CFD analyses to assess the impact of the strip-model approximations and internal deformations on the film-cooling flow. Moreover, testing the proposed methodology on a broader range of HPT rotor blades (or any film-cooled blades) will help to determine its general applicability.

Acknowledgements

Development and applications of digital twins of engine components were carried out as part of the NEXTAIR project, funded by the European Union under Grant Agreement No. 101056732. The views and opinions expressed are, however, those of the author(s) only and do not necessarily reflect those of the European Union or REA. Neither the European Union nor the REA can be held responsible for them.

References

[1] M. Javaid et al. "Industrial perspectives of 3D scanning: Features, roles and it's analytical applications". In: *Sensors International* 2 (Jan. 1, 2021), p. 100114. ISSN: 2666-3511. DOI: 10.1016/j.sintl.2021.100114.

[2] B. Gapinski et al. "Comparison of Different Method of Measurement Geometry Using CMM, Optical Scanner and Computed Tomography 3D". In: *Procedia Engineering*. 24th DAAAM International Symposium on Intelligent Manufacturing and Automation, 2013 69 (Jan. 1, 2014), pp. 255–262. ISSN: 1877-7058. DOI: 10.1016/j.proeng.2014.02.230.

[13] Only such mechanisms are implemented as allowable deformation modes

[3] M. Carta, T. Ghisu, and S. Shahpar. "High-Fidelity Computational Fluid Dynamics Analysis of In-Serviced Shrouded High-Pressure Turbine Rotor Blades". In: *Journal of Turbomachinery* 144.12 (2022). DOI: 10.1115/1.4055267.

[4] M. Carta, T. Ghisu, and S. Shahpar. "Multi-Fidelity Heat Transfer Analysis of Shrouded High-Pressure Turbine Rotor Blades". In: vol. 13B: Turbomachinery — Axial Flow Turbine Aerodynamics. Turbo Expo. June 2023. DOI: 10.1115/GT2023-103789.

[5] M. Carta, T. Ghisu, and S. Shahpar. "Heat Transfer Analysis of Damaged Shrouded High-Pressure Turbine Rotor Blades". In: *International Journal of Turbomachinery, Propulsion and Power* 8.3 (2023). DOI: 10.3390/ijtpp8030024.

[6] G. Bzymek et al. "Computational Fluid Dynamics Study of Erosion on 900 MW Steam Turbine ND-45 Blades Using 3D Scanning". In: *Materials* 17 (Oct. 4, 2024), p. 4884. DOI: 10.3390/ma17194884.

[7] S. Hameed and I. Manarvi. "Using FEM and CFD for Engine Turbine Blades to Localize Critical Areas for Non Destructive". In: *International Journal Of Multidisciplinary Sciences And Engineering* (June 1, 2011).

[8] M. E. Crawford, W. M. Kays, and R. J. Moffat. *Full-coverage film cooling on flat, isothermal surfaces: Data and predictions*. SU-HMT-23. NTRS Author Affiliations: Stanford Univ. NTRS Document ID: 19800007104 NTRS Research Center: Legacy CDMS (CDMS). Jan. 1, 1980.

[9] K. Zhang et al. "An automated method to morph finite element whole-body human models with a wide range of stature and body shape for both men and women". In: *Journal of Biomechanics* 60 (2017), pp. 253–260. ISSN: 0021-9290. DOI: https://doi.org/10.1016/j.jbiomech.2017.06.015.

[10] R. Ando, Y. Ozasa, and W. Guo. "Robust Surface Reconstruction of Plant Leaves from 3D Point Clouds". In: *Plant Phenomics* 2021 (2021). DOI: 10.34133/2021/3184185.

[11] D. Xu et al. "Aerodynamic Design Optimization Of Centrifugal Compressor Blade Using Parametrized Free-Form Deformation". In: *Proceedings of the ASME Turbo Expo*. Vol. 12D. Type: Conference paper. 2024. DOI: 10.1115/GT2024-125778.

[12] Z. Tao et al. "Aerothermal optimization of a turbine rotor tip configuration based on free-form deformation approach". In: *International Journal of Heat and Fluid Flow* 110 (2024). Type: Article. DOI: 10.1016/j.ijheatfluidflow.2024.109644.

[13] J. Alistair, N. Qin, and S. Shahpar. "The Influence of Parameterisation Setup on the Constrained Adjoint Optimisation of Transonic Fan Blades". In: ASME Turbo Expo 2020: Turbomachinery Technical Conference and Exposition. American Society of Mechanical Engineers Digital Collection, Jan. 11, 2021. DOI: 10.1115/GT2020-15352.

[14] S. Shahpar. "Analysis of modern fan manufacturing variations and their links to Jet-engine performance". In: *The Aeronautical Journal* 128.1320 (2024), pp. 273–291. DOI: 10.1017/aer.2023.75.

[15] J. P. Kruth et al. "Computed tomography for dimensional metrology". In: *CIRP Annals* 60.2 (Jan. 1, 2011), pp. 821–842. ISSN: 0007-8506. DOI: 10.1016/j.cirp.2011.05.006.

[16] R. Przysowa et al. "CT Inspection of Cooled Turbine Blades". In: *Journal of KONBiN* 50 (Oct. 2020), pp. 307–331. DOI: 10.2478/jok-2020-0064.

[17] E. Amoiralis and I. Nikolos. "Freeform Deformation Versus B-Spline Representation in Inverse Airfoil Design". In: *Journal of Computing and Information Science in Engineering* 8 (June 1, 2008). DOI: 10.1115/1.2906694.

[18] T. W. Sederberg and S. R. Parry. "Free-form deformation of solid geometric models". In: *Proceedings of the 13th Annual Conference on Computer Graphics and Interactive Techniques*. SIGGRAPH '86. New York, NY, USA: Association for Computing Machinery, 1986, pp. 151–160. ISBN: 0-89791-196-2. DOI: 10.1145/15922.15903.

[19] D. A. Masters et al. "A Geometric Comparison of Aerofoil Shape Parameterisation Methods". In: *54th AIAA Aerospace Sciences Meeting*. AIAA SciTech Forum. American Institute of Aeronautics and Astronautics, Jan. 2, 2016. DOI: 10.2514/6.2016-0558.

[20] R. M. Hicks and P. A. Henne. "Wing Design by Numerical Optimization". In: *Journal of Aircraft* 15.7 (July 1978). Publisher: American Institute of Aeronautics and Astronautics, pp. 407–412. ISSN: 0021-8669. DOI: 10.2514/3.58379.

[21] J. Samareh. "Aerodynamic Shape Optimization Based on Free-Form Deformation". In: 10th AIAA/ISSMO Multidisciplinary Analysis and Optimization Conference. Albany, New York: American Institute of Aeronautics and Astronautics, Aug. 30, 2004. ISBN: 978-1-62410-019-2. DOI: 10.2514/6.2004-4630.

[22] A. de Boer, M. S. van der Schoot, and H. Bijl. "Mesh deformation based on radial basis function interpolation". In: *Computers & Structures*. Fourth MIT Conference on Computational Fluid and Solid Mechanics 85.11 (June 1, 2007), pp. 784–795. ISSN: 0045-7949. DOI: 10.1016/j.compstruc.2007.01.013.

[23] S.S. Sarakinos, E. Amoiralis, and I.K. Nikolos. "Exploring Freeform Deformation Capabilities in Aerodynamic Shape Parameterization". In: *EUROCON 2005 - The International Conference on "Computer as a Tool"*. EUROCON 2005 - The International Conference on "Computer as a Tool". Vol. 1. Nov. 2005, pp. 535–538. DOI: 10.1109/EURCON.2005.1629983.

[24] X. Tang, J. Luo, and F. Liu. "Adjoint aerodynamic optimization of a transonic fan rotor blade with a localized two-level mesh deformation method". In: *Aerospace Science and Technology* 72 (Jan. 1, 2018), pp. 267–277. ISSN: 1270-9638. DOI: 10.1016/j.ast.2017.11.015.

[25] J. Niu, J. Lei, and T. Lu. "Numerical research on the effect of variable droop leading-edge on oscillating NACA 0012 airfoil dynamic stall". In: *Aerospace Science and Technology* 72 (Jan. 1, 2018), pp. 476–485. ISSN: 1270-9638. DOI: 10.1016/j.ast.2017.11.030.

[26] K. Bobrowski et al. "Aerodynamic Shape Optimization Using Geometry Surrogates and Adjoint Method". In: *AIAA Journal* 55.10 (2017), pp. 3304–3317. ISSN: 0001-1452. DOI: 10.2514/1.J055766.

[27] R. Agromayor et al. "Multirow Adjoint-Based Optimization of NICFD Turbomachinery Using a Computer-Aided Design-Based Parametrization". In: *Journal of Engineering for Gas Turbines and Power* 144.41008 (Jan. 21, 2022). ISSN: 0742-4795. DOI: 10.1115/1.4052881. (Visited on 06/21/2025).

[28] S. Shahpar and L. Lapworth. "PADRAM: Parametric Design and Rapid Meshing System for Turbomachinery Optimisation". In: ASME Turbo Expo 2003, collocated with the 2003 International Joint Power Generation Conference. American Society of Mechanical Engineers Digital Collection, Feb. 4, 2009, pp. 579–590. DOI: 10.1115/GT2003-38698.

[29] D. Kraft. *A Software Package for Sequential Quadratic Programming*. Deutsche Forschungs- und Versuchsanstalt für Luft- und Raumfahrt Köln: Forschungsbericht. Wiss. Berichtswesen d. DFVLR, 1988.

[30] *CloudCompare - Open Source project*. URL: https://www.cloudcompare.org/ (visited on 05/07/2025).

[31] P. Virtanen et al. "SciPy 1.0: Fundamental Algorithms for Scientific Computing in Python". In: *Nature Methods* 17 (2020), pp. 261–272. DOI: 10.1038/s41592-019-0686-2.

[32] M. Tezzele et al. "PyGeM: Python Geometrical Morphing". In: *Software Impacts* 7 (2021), p. 100047. ISSN: 2665-9638. DOI: https://doi.org/10.1016/j.simpa.2020.100047.

[33] Blender Online Community. *Blender - a 3D modelling and rendering package*. Stichting Blender Foundation, Amsterdam: Blender Foundation, 2018. URL: http://www.blender.org.